Numerical analysis of a water mist spray: The importance of various numerical and physical parameters, including the drag force

Yuanjun Liu [a, b], Tarek Beji [b], Martin Thielens [b], Zhi Tang [a*, c], Zheng Fang [a*, c], Bart Merci [b]

[a] *School of Civil Engineering, Wuhan University, Wuhan, Hubei 430072, China*

[b] *Department of structural engineering and building materials, Ghent University-UGent, B-9000 Ghent, Belgium*

[c] *Engineering Research Center of Urban Disasters Prevention and Fire Rescue Technology of Hubei Province, Wuhan, China*

Abstract

This paper presents a comprehensive set of numerical simulations for the characterization of a water mist spray emerging from a nozzle positioned at 2.2 m from floor level and operating at a pressure of 1.0 MPa. The droplet volume-median diameter is about 90 μm and the spray half-angle is around $42°$. The spray shape is visualized using a laser sheet and the water flux density distribution on the ground is measured with a 'bucket' test. An initial comprehensive numerical study using the Fire Dynamics Simulator (FDS) has been carried out by varying several numerical and physical models and parameters (e.g., cell size and turbulence modelling). The simulated sprays were very narrow (in comparison to the actual spray), yielding overestimations of the peak water flux density at floor level by about 430% (on average). Subsequently, it was found that there is a significant impact of the drag force modelling because the spray at hand is dense (near the nozzle). An ad-hoc reduction of the drag coefficient to a constant value leads to better results. The current study calls upon new developments for droplet aerodynamic modelling in dense sprays.

Keywords: CFD; water mist; nozzle; drag reduction

Nomenclature

A_0	bucket area (m^2)
C_d	drag coefficient between the liquid droplets and the gas (-)
$C_{d,0}$	single particle drag coefficient (-)

d	spray width near the nozzle (m)
D	particle diameter (μm)
$D_{V,0.50}$	volume-median diameter (μm)
$F_{V,\mathrm{D}}(\mathrm{D})$	Cumulative Volume Fraction (CVF) of water droplets (-)
F	hydrodynamic force of the trailing particle (N)
F_0	hydrodynamic force of the isolated particle (N)
$\vec{g}$	gravitational acceleration (m/s^2)
L	inter-particle spacing (μm)
m_d	droplet mass (kg)
N_p	number of computational droplets per second (s^{-1})
$\dot{q}$	water volume flow rate of the nozzle (L/min)
$\dot{q}''$	local water flow density at a certain point ($L/min/m^2$)
$\dot{q}''_{max}$	maximum local water flux density ($L/min/m^2$)
$\overline{\dot{q}''}$	average water flux density in each bucket ($L/min/m^2$)
Re	particle Reynolds number (-)
t	steady-state time period of the spray (s)
$t_{(h)}$	time at which droplets reach the distance h from the nozzle (min)
$\vec{u}$	gas phase velocity (m/s)
$\overrightarrow{u_d}$	droplet velocity (m/s)
v_0	initial velocity of a droplet (m/s)
V	the collected water volume in the bucket (L)
$V_{water\ (h)}$	volume of water up to a distance h from the nozzle (L)
$\mathrm{V}_{\text{spray enveloppe (h)}}$	volume of the spray envelope up to a distance h from the nozzle (L)
W	non-dimensional, non-disturbed wake velocity at the center of the trailing particle (-)

Greek symbols

α	local water volume fraction (-)

$\bar{\alpha}$	average water volume fraction near the nozzle (-)
γ	droplet size distribution width parameter (-)
ΔP	water pressure at the nozzle (MPa)
Δx	cell size (cm)
ε	deviation between simulation and experimental results (-)
θ	(half) spray angle (°)
μ	dynamic gas phase viscosity (Pa·s)
ρ	water density (kg/L)
$\bar{\rho}$	gas phase density (kg/m^3)

1 Introduction

Water mist systems are widely accepted for fire control and suppression in buildings because of their high cooling efficiency and oxygen dilution [1], which have been experimentally investigated in, e.g., [2-4]. Numerical modeling serves as another effective and less expensive means to explore the performance of water mist in different fire scenarios [3-7]. Numerical simulations also serve as a 'support' for experiments where the flow field (e.g., air entrainment) is difficult to measure. However, results from simulations can only be trusted when the modeling is proven accurate enough by validation against experiments. Often, such validation work is performed directly for the interaction between a water spray and a fire-driven flow. However, it is considered crucial to proceed first with the numerical characterization of a single water mist nozzle in the absence of any fire-driven flow as in [8-11]. Husted et al. [8] compared FDS results in to the experimental data of a hollow cone water mist spray in terms of droplet velocity and water concentration. Significant deviations were partially attributed to turbulence modelling. The effects of the cell size, the turbulence model, the particle injection rate and the spray angular distribution were examined in detail in [9, 10, 12, 13]. It was found that all these aspects have an influence on the numerical characterization of the spray. However, the number of injected computational droplets per second is particularly important in that the default number of 5,000 s^{-1} had to be

increased to a few millions in order to minimize the statistical error. Apart from the droplet size and velocity [8-10, 12, 14-16], the water flux density distribution on the ground was also used to validate the CFD simulations, showing a good agreement with the experiments [11, 17].

In order to increase the predictive capability of CFD models for spray dynamics, there is still a strong need to carry out more validation. In this paper, such an assessment is performed based on the overall shape of the spray and the water flux density distribution at floor level, as measured in the bucket tests. This numerical work has initially been thought to be, to some extent, a 'formality' prior to the more complex scenarios involving a fire-driven flow. However, it has been observed that the spray envelope in the simulation is significantly narrower than in the experiment. This has triggered the comprehensive numerical study reported in this paper and which addressed the influence of a wide range of numerical (e.g., the gas phase cell size and the number of particles per second) and physical parameters and models (e.g., turbulence). Ultimately, the study has led to highlight the importance of the drag force model for the case at hand, which can be explained by strong inter-particle aerodynamic interactions under 'dense' conditions.

2 Experimental set-up and results

2.1 Parameters at the injection and spray shape

The orifice diameter of the water mist nozzle considered herein (see Fig. 1) is 1.8 mm. In order to measure the water volume flow rate under the operating pressure ΔP =1.0 MPa, a container was used to collect all the water spray induced from the nozzle for 3 minutes and the measured total water volume was divided by the time period (3 min). The measurement was repeated three times, and the average calculated water volume flow rate was 1.0 L/min.

The initial velocity of a droplet near the nozzle can be estimated from:

$$v_0 = C\sqrt{\frac{2000\Delta P}{\rho}} \qquad (1)$$

where ρ is the water density. The parameter C is a factor used to account for the friction losses in the nozzle. It has not been determined experimentally but, typically, the value of C varies between 0.5 and 1, which corresponds to initial velocity values between 22 and 45 m/s. A sensitivity analysis on the latter will be performed in order to examine the influence of the uncertainty in v_0 on the overall numerical spray characterization.

The water mist nozzle produces a solid cone of fine water droplets with a spray half-angle of $42°$, as shown in Fig. 2 (a). The spray picture, as shown in Fig. 2 (b), was taken by means of a laser sheet and shows the overall shape of the spray from the nozzle to the ground. The picture was taken in a 2.2 m-high reduced-scaled tunnel. Due to the limited space inside the tunnel, the front view of the laser image is not available. However, it can still be clearly observed that the spray exhibits a conical shape up to a certain distance from the nozzle before the gravitational force becomes dominant over the initial momentum and the spray shape becomes close to cylindrical. This is similar to the observations in [8] for a full cone water mist spray using the High Speed Camera.

The maximum diameter of the cone, i.e., the diameter of the cylinder from the observation in Fig. 2 (b), is estimated as $1.26 \pm 0.18\ \mathrm{m}$ (with the height of the cone spray part of $0.7 \pm 0.1\ \mathrm{m}$).

Fig. 1. The experimental nozzle geometry.

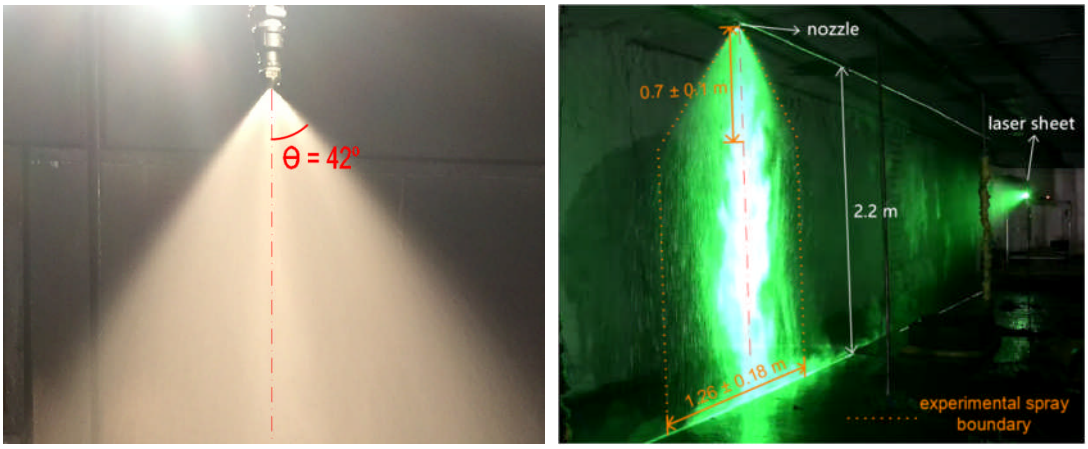

(a) in sunlight (b) laser sheet visualization

Fig. 2. Picture (left) and laser sheet visualization (right) of the water mist emerged by the nozzle.

2.2 Drop size distribution (DSD)

The drop size distribution (DSD) was measured by the laser particle analyzer, capturing all the droplets in the spray zone in the horizontal plane 1 m below the nozzle, as prescribed in NFPA 750 [18]. According to the scattering of the light by the droplets, the diameters of all the droplets passing through the laser plane at a time point are collected and the DSD is calculated. The latter is expressed in terms of Cumulative Volume Fraction (CVF), as shown in Fig. 3. The CVF of the droplets agrees well with the Rosin-Rammler-lognormal curve [9]:

$$F_{V,D}(D) = \begin{cases} \frac{1}{\sqrt{2\pi}} \int_0^D \frac{1}{\sigma D'} exp\left(- \frac{\left[ln\left(D'/D_{V,0.50}\right) \right]^2}{2\sigma^2} \right) dD' & \left(D \le D_{V,0.50}\right) \\ 1 - exp\left[- ln(2) \left(\frac{D}{D_{V,0.50}} \right)^{\gamma} \right] & \left(D > D_{V,0.50}\right) \end{cases}$$

$$\sigma = \frac{2}{\sqrt{2\pi}(ln\,2)\gamma} \qquad (2)$$

where $F_{V,\mathrm{D}}(\mathrm{D})$ is the CVF, γ is the distribution width parameter and $D_{V,0.50}$ is the volume-median diameter, which is about 90 μm for the case at hand.

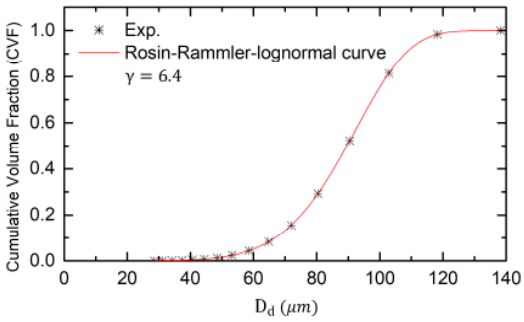

Fig. 3. The measured Cumulative Mass Fraction and curve fitting with a Rosin-Rammler-lognormal distribution (Eq. (2)).

2.3 Water flux density distribution

In order to obtain the water flux density distribution at floor level, the bucket tests were conducted. As shown in Fig. 4, the nozzle was placed inside a hood and there are 8×8 buckets in total right under it. The vertical distance from the nozzle to the ground is same as in Fig. 2 (b), to be 2.2 m. The bucket size is 20 mm × 20 mm, made of 3 mm thick PMMA. The average water flux density, $\overline{\dot{q}''}$ (in $\mathrm{L/min/m^2}$), in each bucket is calculated as:

$$\overline{\dot{q}''} = \frac{V}{t \cdot A_0} \tag{3}$$

where V (in L) is the collected water volume in the bucket; A_0 (in $\mathrm{m^2}$) is the collected area of the bucket ($A_0 = 4.0 \times 10^{-2}\ \mathrm{m^2}$); t (in min) is the time period and is chosen as 90 min. As the unsteady spray here is only around 3 s after the activation, it is negligible during the experiment. The repeatability test was also conducted. Then the water flux density distribution results on the ground based on the values of $\overline{\dot{q}''}$ in each bucket are obtained, see Fig. 4 (d).

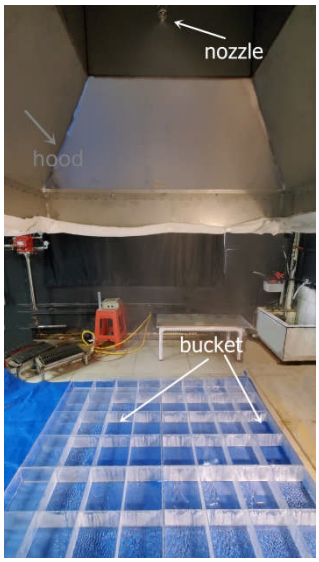

(a) Picture of the experiment (front view)

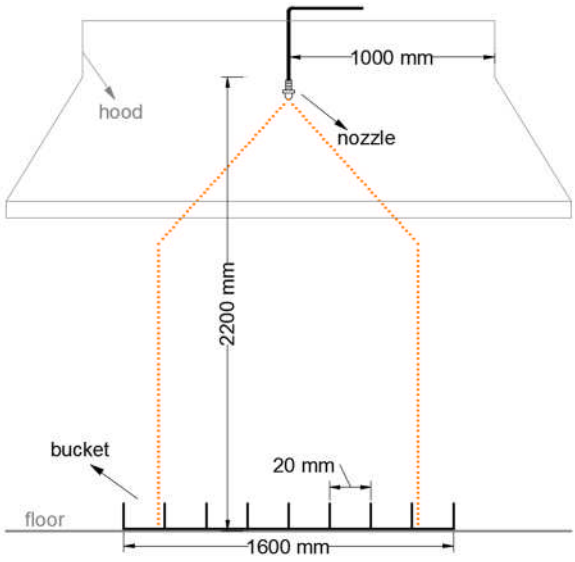

(b) Front view

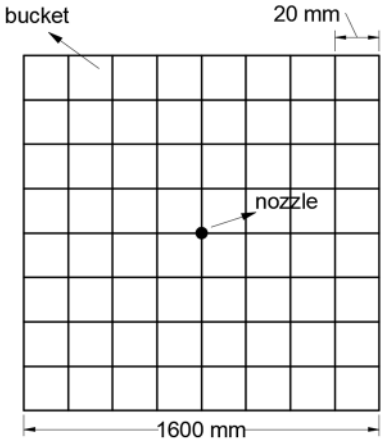

(c) Top view

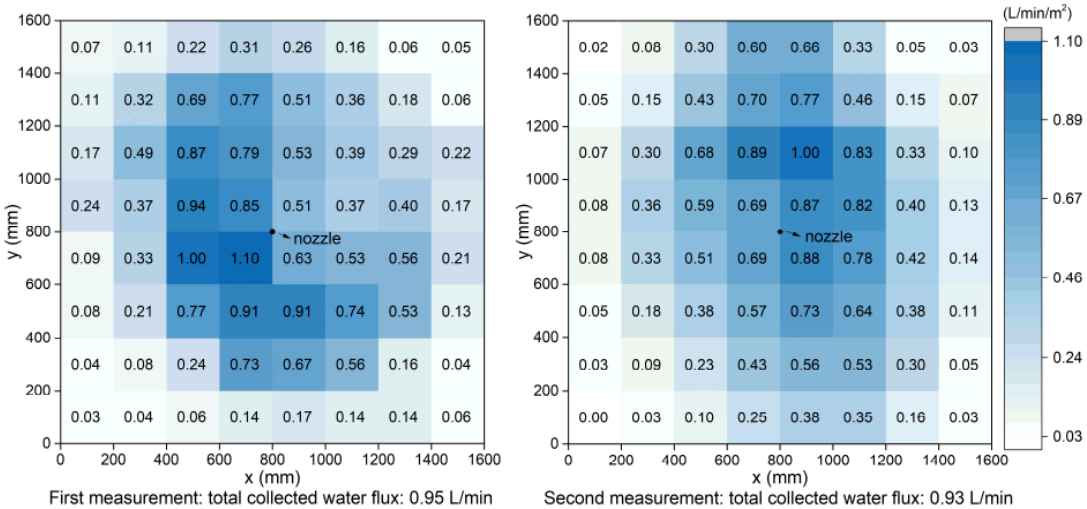

(d) Water flux density distribution results

Fig. 4 Front view (a, b) and top view sketch (c) of the measurements, and measured values of the water flux density distribution (d) in the bucket tests.

It can be observed in Fig. 4 (d) that the total water flux collected in all the buckets

are about 5% to 7% less than the water flux of the nozzle (1.0 L/min), as there is some water falling on the ground out of the bucket scope. Besides, it should be noted that it is difficult to adjust the nozzle to the exact vertical direction (the nozzle orientation was adjusted slightly from the first measurement to the second one), therefore the location of the maximum $\overline{\dot{q}''}$ values do not appear right under the nozzle.

3 Mathematical models

The computational fluid dynamics (CFD) package used in this study is the Fire Dynamics Simulator, FDS 6.7.5 [19]. Large Eddy Simulation (LES) and the Lagrangian approach are adopted to describe respectively turbulence and water droplet transport in FDS. The governing equations and solution methods are described in [20]. For clarity, only the most relevant mathematical models for the present spray simulation study are described here.

3.1 Lagrangian particle model

The momentum conservation equation of a single spherical droplet is [20, 21]:

$$m_d \frac{d\overrightarrow{u_d}}{dt} = m_d \vec{g} - \frac{\pi D^2}{8} \bar{\rho} C_d (\overrightarrow{u_d} - \vec{u}) |\overrightarrow{u_d} - \vec{u}| \qquad (4)$$

where m_d, $\overrightarrow{u_d}$, D refer to the droplet mass, velocity and diameter, respectively; $\vec{g}$ is the gravitational acceleration; $\bar{\rho}$ and $\vec{u}$ are the resolved gas phase density and velocity in a cell occupied by the droplet; C_d represents the drag coefficient between the liquid droplet and the gas, which is given by:

$$C_d = \begin{cases} 24/Re & Re < 1 \\ 24\,(0.85 + 0.15Re^{0.687})/Re & 1 < Re < 1000 \\ 0.44 & Re > 1000 \end{cases} \qquad (5)$$

where Re is the droplet Reynolds number:

$$Re = \frac{\bar{\rho}|\overrightarrow{u_d} - \vec{u}|D}{\mu} \qquad (6)$$

where μ is the dynamic gas phase viscosity.

3.2 Drag reduction

In dilute sprays only two-way coupling is considered between the gas and the

particles. This means that each particle interacts with the carrier fluid individually. The momentum lost from a particle is added to the fluid and vice versa. However, if the spray is dense enough, the individual particles affect each other through aerodynamic interactions [22]. These effects cannot be captured explicitly by the current Eulerian-Lagrangian model for two reasons. First, the Lagrangian particles occupy no volume in the Eulerian space. Second, the separation lengths would be of sub-grid scale in most practical simulations. In a configuration where two particles with the same diameter are directly in line, the separation distance, i.e. the ratio of the inter-particle spacing to the particle diameter, L/D, is obtained from the local particle volume fraction, α [23, 24]:

$$L/D = (\pi/6\alpha)^{1/3} \qquad (7)$$

Here, local quantities are averaged over a single computational cell.

The aerodynamic interactions start to have an effect when the average particle spacing is less than 10 diameters [23, 24], i.e. $L/D < 10$, which corresponds to the particle volume fraction $\alpha > 5 \times 10^{-4}$ according to Eq. (7). In this case, i.e., a dense spray, the reduction of the drag force on the second particle is modeled in FDS by [20]:

$$C_d = C_{d,0}\frac{F}{F_0} \qquad (8)$$

where $C_{d,0}$ is the single particle drag coefficient and F/F_0 is the hydrodynamic force ratio of the trailing particle to an isolated particle:

$$\frac{F}{F_0} = W\left[1 + \frac{Re}{16}\frac{1}{(L/D-1/2)^2}exp\left(-\frac{Re}{16}\frac{1}{(L/D-1/2)}\right)\right] \qquad (9)$$

where Re is the single particle Reynolds number and W is the non-dimensional, non-disturbed wake velocity at the center of the trailing particle:

$$W = 1 - \frac{C_{d,0}}{2}\left[1 - exp\left(-\frac{Re}{16}\frac{1}{(L/D-1/2)}\right)\right] \qquad (10)$$

In reality, the spray is not monodisperse and the separation distance between the interacting particles varies. In the simulation, the drag reduction factor in Eq. (8) is only used when the local droplet volume fraction exceeds 10^{-5}. The drag reduction model is turned on by default.

4 Computational setup and the problems to be solved

The cases were simulated with a rectangular computational area of 2.2 m high, 1.6 m wide and 1.6 m deep, as shown in Fig. 5 (a). The boundary condition on the sides of the domain was set to 'open'. Two 'inert' walls represent the ceiling and the ground. The nozzle was placed 60 mm below the ceiling, as in the experimental set-up. In order to simulate the bucket test in the experiment (Fig. 4), a quantity called 'AMPUA' (Accumulated Mass Per Unit Area, given in kg/m^2) for the particle (water) was monitored in the simulations, with the statistics as 'SURFACE INTEGRAL'. The average water flux density, $\overline{\dot{q}''}$, over each device is calculated as:

$$\overline{\dot{q}''} = 60 \times \frac{AMPUA}{\rho \cdot t} \qquad (11)$$

where t (s) is the steady-state time period in the simulation. The simulation time was chosen to be 10 s and only the results in the last 8 s were collected for the data analysis, to ensure that the simulation has reached steady state, as confirmed by temporal profiles of the water flux density and the gas velocity at several positions in the computational domain (not shown here).

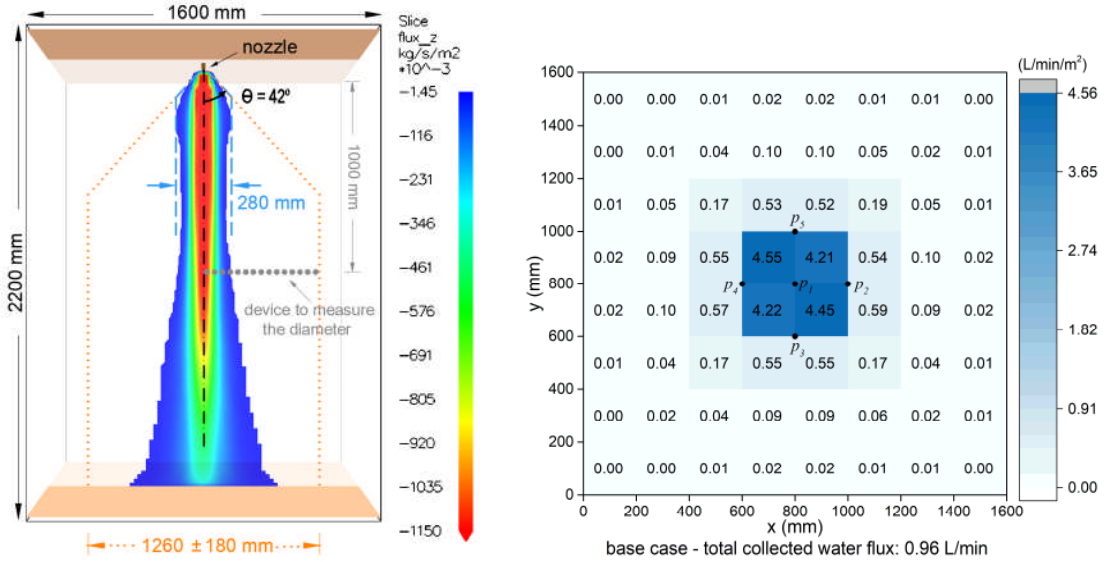

(a) Time-averaged water flux density slice (b) Water flux density distribution on the ground

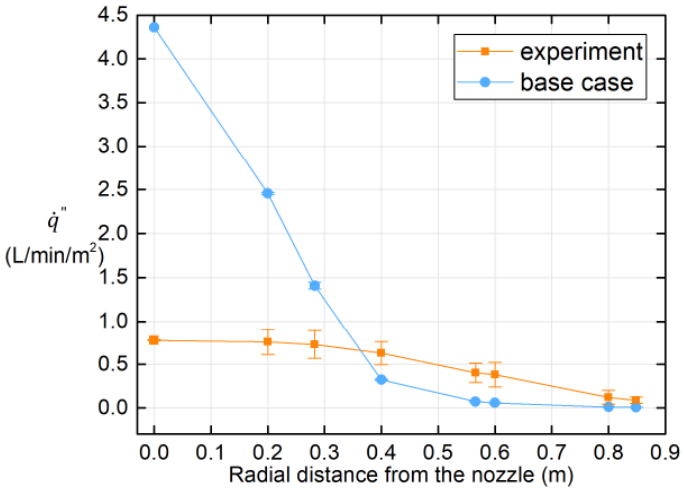

(c) Water flux density on the ground along the radial direction of the experiment and the base case

Fig. 5. Comparison between the simulation results of the base case (see in Table 1) and the experimental results (indicated by the orange dashed lines).

The input variables to the model include the water flow rate (1.0 L/min) and the droplet size distribution ($D_{V,0.50} = 90\ \mu m,\ \gamma = 6.4$), as introduced in the section 2. The minimum diameter, D_{min}, and the maximum diameter, D_{max}, were set as 10 μm and 1000 μm, respectively. As the DSD was measured 1 m below the nozzle in the experiment, the droplet diameters were also monitored in the simulation using some measurement points, with 40 mm intervals (see dotted line labeled 'device to measure the diameter' in Fig. 5 (a)). Each 'numerical' device consists of a 1 cm-diameter sphere. Each droplet crossing the sphere (during a specified sampling period) is recorded and a histogram of droplet size distribution is obtained and post-processed in order to calculate the volume-median diameter. Fig. 6 shows that at 1 m below the nozzle, the value of $D_{V,0.50}$ increases from around 75 μm to 107 μm in the radial direction, which is consistent with the average value of $D_{V,0.50} = 90\ \mu m$ measured experimentally. The volume-median diameter did not vary substantially from the nozzle up to 1 m further downstream. Furthermore, the lower $D_{V,0.50}$ recorded in the centerline (as shown in Fig. 6) can be explained by the fact that the smallest droplets are entrained in the spray center, as discussed in [12].

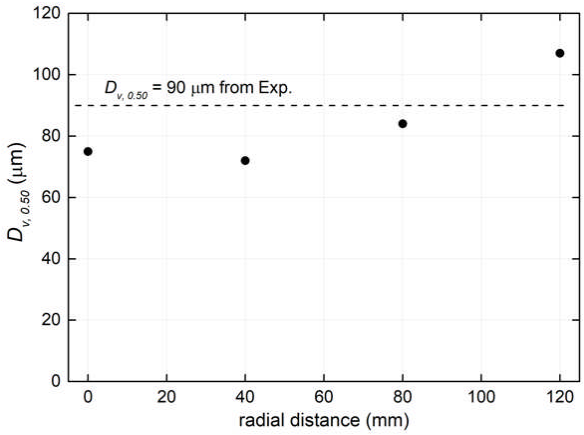

Fig. 6. Simulation results of $D_{V,0.50}$ at measurement points 1 m below the nozzle. Locations of the measurement points are shown in Fig. 5 (a).

The initial velocity of a droplet has been taken as 20 m/s in the base case. A higher value of 42 m/s has also been considered in order to cover the full range of possible values between 0.5 and 1 for the friction loss coefficient, *C*, at the nozzle, which has not been characterized experimentally.

A sensitivity study (see sections 5.1) has been carried out as well on the value of N_p (the number of computational droplets per second) and the cell size, Δx. In the base case, $N_p = 2 \times 10^5\ s^{-1}$ and $\Delta x = 2$ cm, as shown in Table 1. The other parameters are given the default values in FDS.

Table 1 Parameters of the base case

Parameter	Value	Description
N_p	$2 \times 10^5\ s^{-1}$	Particles inserted to the simulation per second
Δx	2 cm	Cell size
v_0	20 m/s	The initial velocity of droplets
θ	42°	Spray angle
SPS	Gaussian (by default)	Spray Pattern Shape
TM	the modified Deardorff model (by default)	Turbulence Model
DRF	ON (by default)	Drag reduction factor

Fig. 5 (b) gives the water flux density distribution of the base case on the ground level based on Eq. (11). In order to compare the distribution results between the experiment and the base case much clearer, the water flux density along the radial direction is also given in Fig. 5 (c). The values in Fig. 5 (c) are deduced based on Fig. 5 (b). For example, for the radial distance of 0 m from the nozzle, the value of 4.36 $L/min/m^2$ is the average result of the four buckets (4.21 $L/min/m^2$, 4.45 $L/min/m^2$,

4.22 $L/min/m^2$ and 4.55 $L/min/m^2$) around point p_1 in Fig. 5 (b). For the radial distance of 0.2 m from the nozzle, the value of 2.45 is the average result of points p_2 ~ p_5. Similarly, the experiment results in Fig. 5 (c) can be deduced based on the average result of the two tests in Fig. 4 (d). It is clear in Fig. 5 (c) there tend to be more water amount gather in the field right under the nozzle.

The iso-contour line, used to define the boundary of the spray, is set to $2\% \times \dot{q}''_{max}$ in this paper, which is $2\% \times 4.36\ L/min/m^2$ for the base case (see in Fig. 5 (c)). Fig. 5 (a) shows the time-averaged water flux density slice in the vertical mid-plane during the steady period. It can be observed that the spray width, d, is nearly 0.28 m near the nozzle. The experimental spray boundary is also indicated, as a dashed orange line, in order to make the comparison clearer with the simulation results. The results show that the experimental spray width of 1.26 ± 0.18 m (as marked in Fig. 2 (b)) is approximately 3.8 times larger than the simulated spray width of 0.28 m. This is a very large deviation. In all, the spray shape in the simulation is significantly narrower than in the experiments.

In order to verify that the results are indeed steady, the simulated time duration has been increased from 8 s (base case) to 58 s, and there was nearly no deviation in d (not shown). Hence, this cannot explain the strong deviation as observed in Fig. 5, while the required CPU time was nearly 8.1 times longer than for the base case. Therefore, the simulation time has been set to 10 s for all cases in the present study, as it has been considered sufficient.

Furthermore, the effect of the wall (at 0.75 m from the nozzle, see Fig. 2 (b)) was considered in an additional simulation. The obtained time-averaged water flux density at the centerline displayed in Fig. 7 is similar to the results displayed in Fig. 5 (a) for the base case without a wall. One can conclude that the effect of the latter on the spray shape and the droplet dynamics is marginal. Also, the effect of the hood in Fig. 4 (a) can also be neglected.

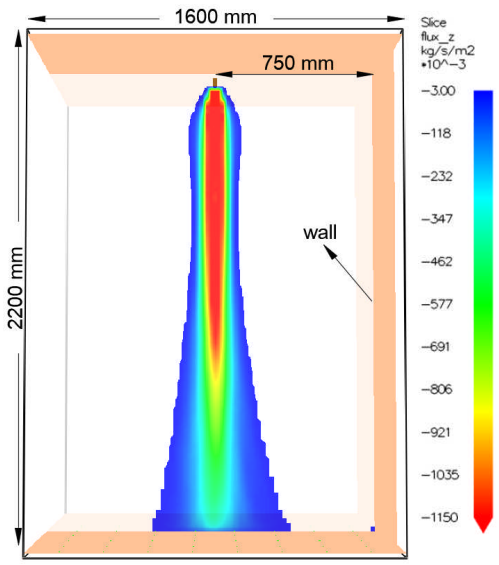

Fig. 7 Time-averaged water flux density slice (considering the effect of the wall 0.75 m from the nozzle)

At this point it is concluded that there are substantial differences in the spray shape and the water flux distribution on the ground between the simulation with the default set-up (base case in Table 2) and the experimental data. In order to better 'reproduce' the experimental spray shape, an extensive sensitivity analysis is carried out in the following section.

5 Results and discussion

Table 2 presents the list of all the simulations and the corresponding results in terms of spray width and water flux distribution at floor level. Deviations of each simulation result from the experimental results are also given. They are calculated as $\varepsilon = 100\% \times (\text{experimental value} - \text{numerical value})/\text{experimental value}$. ε_q is based on the average value of the deviations in various radial distances from the nozzle. Each simulation was run on a single processor. In Cases 1 to 9, the sensitivity study focuses on the particle injection rate, the grid size, the initial velocity and the spray angle. In Cases 10 and 11, the spray pattern shape and the turbulence model are varied from the default set-up, respectively. Finally, the effect of the drag reduction is further evaluated in Case 12 (deactivating the drag reduction as described in Eqs. (7-9)) and Cases 13 to 28 (replacing Eq. (4) by fixed values of the drag coefficient). The results of the total water flux collected in all buckets are also shown.

Table 2 Results for the water flux density distribution and spray diameter, as well as relative deviations from the experimental values

Case No.	Changed parameters (compared to the base case)	Results and errors					
		d (m)	ε_d (%)	$\dot{q}''_{max}$ $(L/min/m^2)$	$\varepsilon_{q_{max}}$ (%)	ε_q (%)	Total water flux in all buckets (L/min)
Base case*	/	0.28	77.8	4.36	-459.0	-146.9	0.96
1	$N_p = 5 \times 10^3\ s^{-1}$	0.33	73.8	3.30	-323.1	-113.0	0.98
2	$N_p = 5 \times 10^4\ s^{-1}$	0.28	77.8	3.96	-407.7	-133.9	0.97
3	$N_p = 5 \times 10^5\ s^{-1}$	0.27	78.6	4.59	-488.5	-154.3	0.95
4	$N_p = 8 \times 10^5\ s^{-1}$	0.28	77.8	4.22	-442.8	-144.5	0.86
5	$\Delta x = 4$ cm	0.31	75.4	4.63	-493.6	-157.5	0.95
6	$\Delta x = 1$ cm	0.28	77.8	4.29	-451.8	-143.7	0.98
7	$v_0 = 42\ m/s$	0.38	69.8	4.14	-430.8	-137.4	0.95
8	$\theta = 60°$	0.36	71.4	4.31	-452.6	-145.8	0.97
9	$\theta = 80°$	0.40	68.3	4.49	-475.6	-151.4	0.97
10	SPS = Uniform	0.36	71.4	4.34	-456.4	-146.7	0.97
11	TM = Dynamic Smagorinsky Model	0.28	77.8	2.84	-264.1	-95.0	0.93
12	DRF = OFF	0.24	81.0	4.39	-462.8	-147.8	0.96
13	Cd = 0.94	0.40	68.3	5.93	-660.3	-195.0	0.97
14	Cd = 3.0	0.12	90.5	5.24	-571.8	-176.8	0.97
15	Cd = 2.0	0.20	84.1	5.64	-623.1	-187.4	0.98
16	Cd = 1.0	0.37	70.6	5.92	-659.0	-194.8	0.97
17	Cd = 0.9	0.40	68.3	5.98	-666.7	-196.3	0.97
18	Cd = 0.8	0.47	62.7	5.94	-661.5	-195.3	0.97
19	Cd = 0.7	0.53	57.9	5.90	-656.4	-194.3	0.97
20	Cd = 0.6	0.60	52.4	5.63	-621.8	-187.3	0.96
21	Cd = 0.5	0.70	44.4	5.13	-557.7	-174.3	0.97
22	Cd = 0.4	0.86	31.7	4.11	-426.9	-146.5	0.97
23	Cd = 0.3	1.12	11.1	2.78	-256.4	-105.3	0.96
24	Cd = 0.2	1.58	-25.4	1.63	-109.0	-53.5	0.94
25	Cd = 0.1	1.70	-32.8	0.90	-16.1	-15.5	0.86
26	Cd = 0.15	1.60	-27.0	1.20	-54.0	-24.3	0.92
27	SPS = Uniform Cd = 0.3	1.60	-27.0	0.69	10.9	19.0	0.96
28	TM = Dynamic Smagorinsky Model Cd = 0.15	1.60	-27.0	1.19	-52.6	-24.7	0.92

* See Table 1.

5.1 Effects of particle injection rate, grid size

Fig. 8 (a) shows the influence of N_p on the computational time (CPU time), for the base case and Cases 1 to 4, in which only the value of N_p varies. The CPU time first shows a slight decrease as N_p increases from $5 \times 10^3\ s^{-1}$ to $5 \times 10^4\ s^{-1}$, and then increases continuously with increasing N_p, up to $8 \times 10^5\ s^{-1}$. This is a similar observation as in [9], where it has been explained by the fact that more time is required to reach numerical convergence when coupling the liquid and gas phases. The deviations in spray width near the nozzle (d), and water flux distribution results on the ground ($\dot{q}''_{max}$ and $\dot{q}''$), are also shown. The deviations do not change significantly when N_p increases from $2 \times 10^5\ s^{-1}$ to $8 \times 10^5\ s^{-1}$. Therefore, $N_p = 2 \times 10^5$ is considered to provide a fairly converged result within a reduced computational time. It should be noted that the significant differences between the experimental measurements and the simulation results for the base case (section 4), do not disappear with higher N_p. This means that the CFD simulation has reached convergence and could be 'trusted' when N_p is increased up to $2 \times 10^5\ s^{-1}$, although the deviations with the experimental results are effectively smaller in $N_p = 5 \times 10^3\ s^{-1}$ and $N_p = 5 \times 10^4\ s^{-1}$, as shown in Fig. 8 (a).

In a similar way, Fig. 8 (b) presents the influence of the cell size, Δx, on the CPU time, deviations of the spray width and the flux distribution simulation results from the experiments, comparing the base case to Cases 5 and 6. The CPU time increases monotonically from about 1.0 h to 387.4 h as the mesh is refined from 4 cm to 1 cm. The deviations in d, $\dot{q}''_{max}$ and $\dot{q}''$ are nearly constant for the cell size of 2 cm and 1 cm. Considering the CPU time and the 'accuracy' of the simulation results, $\Delta x = 2\ \mathrm{cm}$ has been chosen as cell size. Strictly speaking, $\Delta x = 2\ \mathrm{cm}$ does not ensure mesh convergence, but it is clear that that discretization errors and uncertainties associated with the mesh cannot (solely) explain the substantial deviations with the experimental data.

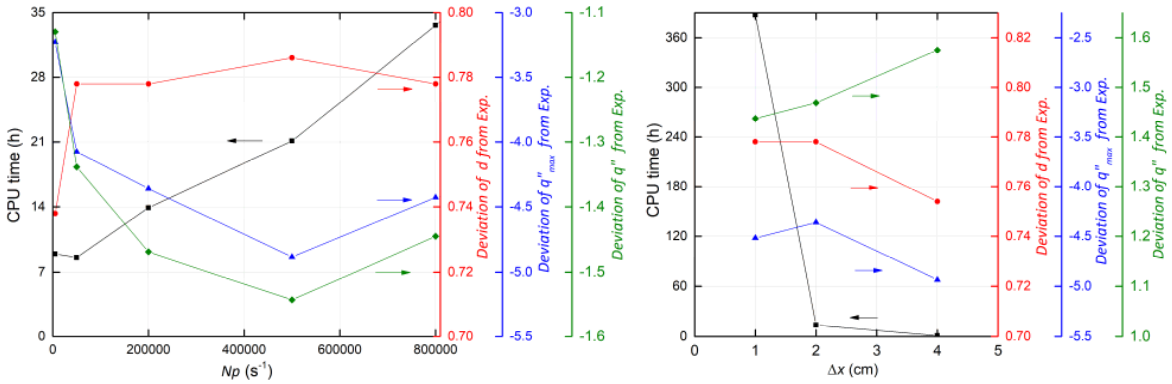

(a) Influence of the particle injection rate, N_p (b) Influence of the cell size, Δx

Fig. 8. Influence of N_p (left) and mesh cell size Δx (right) on the computational time, spray width (ε_d) and water flux distribution results ($\varepsilon_{q_{max}}$ and ε_q).

5.2 The effects of initial velocity, spray angle and spray pattern shape

Based on the analysis above, the values of $N_p = 2 \times 10^5\ s^{-1}$ and $\Delta\mathrm{x} = 2\ \mathrm{cm}$ have been used in Cases 7 to 27. As the droplet velocity could only be estimated (from Eq. (1)), a higher initial velocity of 42 m/s is considered in Case 7 (which corresponds to C = 0.94 in Eq. (1)) to explore the sensitivity of the results to the initial velocity. As expected, a wider spray shape is obtained, but the deviations from the experimental results still remain substantial (69.8%, -430.8% and -137.4% for d, $\dot{q}"_{max}$ and $\dot{q}"$, respectively). Varying the input velocity from 20 m/s to 42 m/s (i.e., more than double) changes the results for the spray width, d, by only 8.0%. Therefore, the exact value of the velocity here does not have a strong effect on the results and is not the focus of the present paper.

Cases 8 and 9 were conducted to quantify the influence of the spray angle. The wider spray angles ($60°$ and $80°$) increase d by about only 6.4% and 9.5%, still yielding significant deviations from the experimental results (71.4% and 68.3%, respectively). Hence also the spray angle can be ruled out as essential parameter and is not the focus of the present paper.

The influence of the spray pattern shape, i.e., angular probability distribution, was thoroughly discussed in [9]. Similarly, a Uniform distribution is prescribed here (Case 10), as opposed to the default Gaussian distribution. The value of d increases by only

6.4% in comparison to the base case, and the deviations with the experiments remain substantial. A combination of a wider angle (e.g. $60°$ to $80°$ as in Cases 8 and 9) with a Uniform distribution does not significantly improve the results (not shown).

5.3 The effects of the turbulence model

FDS version 6.6.0 uses the modified Deardorff model of turbulent viscosity by default. However, thus far the simulation results do not agree well with the experimental data. In the high pressure water mist nozzle simulations of Sikanen et al. [10], it was found that the dynamic Smagorinsky model provided an overall better agreement than the modified Deardorff model in terms of droplet velocity and mist flux profiles. Beji et al. [9] also compared the simulation results of these two turbulence models, and the results using these two models did not show significant differences. The assessment of the numerical modeling in [9, 10] was based on several measurement points (in terms of water flux and droplet diameter and velocity) at a certain distance below the nozzle. In this work, we further explore the influence of the dynamic Smagorinsky model on the spray shape and water flux density distributions on the floor (Case 11). The water flux density profile shown in Fig. 9 (a) is similar to the results with the modified Deardorff model (see Fig. 5 (a)) near the nozzle, showing the same d of 0.28 m. Further downstream, the droplets tend to travel further away from the vertical centerline of the spray with the DS turbulence model. This is believed to be due to the fact that the DS model 'promotes' more the turbulent dispersion of droplets that the modified Deardorff model, as highlighted and discussed in [12].

As a consequence, the water spray pattern results on the ground in Fig. 9 (b) show smaller deviations from experiments in comparison to the modified Deardorff model, with the deviation of $\dot{q}''_{max}$ decreasing from -459.0% to -264.1%, and the deviation of $\dot{q}''$ decreasing from -146.9% to -95.0%. However, in the experiments the spray shape (Fig. 2 (b)) tends to be a cone from the nozzle to a distance of about 0.7 ± 0.1 m below the nozzle, with the diameter of nearly 1.26 m, with little widening below this height

(i.e., the shape becomes cylindrical). This is significantly different from what is observed in Fig. 9 (a), where the spray width is only about 0.28 m at 0.7 m below the nozzle and the spray further widens downstream. In other words, it is misleading to look only at the values at floor level to assess the results. Moreover, the required CPU time is 49.6% longer with the dynamic Smagorinsky model than with the modified Deardorff model. Hence, while there is clear impact from the turbulence model, as could be expected for the small droplets at hand, there is no strong reason to abandon the default modified Deardorff model for the case at hand, as this model leads to the correct qualitative shape of the spray. Nevertheless, also in the next section, a brief comparison to results with the dynamic Smagorinsky turbulence model will be made.

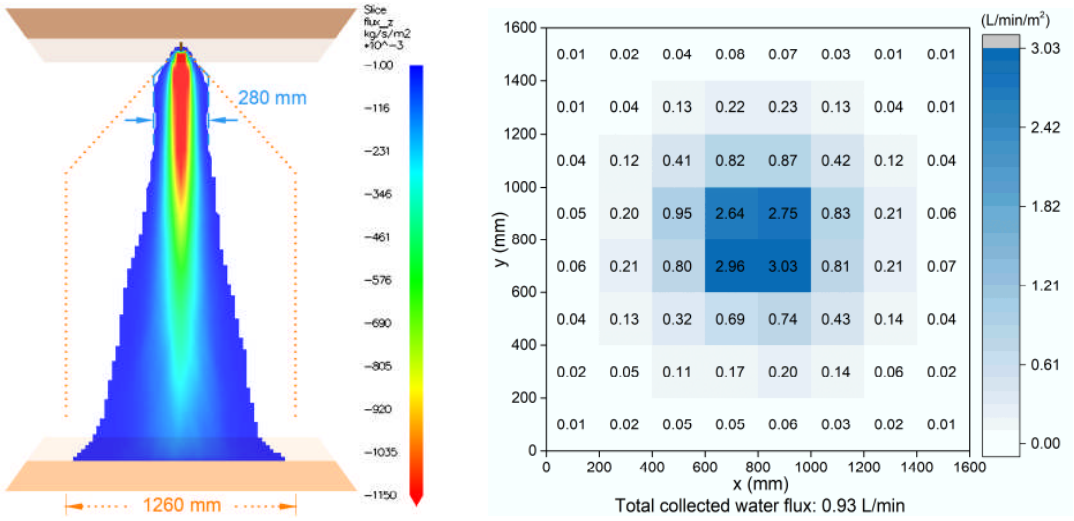

(a) Time-averaged water flux density slice (b) Flux density distribution on the ground

Fig. 9. Simulation results using the dynamic Smagorinsky model (Case 11). The orange dashed lines denote the experimental results.

5.4 The discussion on the drag coefficient

At this stage, despite the extensive sensitivity analysis for the numerical characterization of the spray at hand, none of the settings have produced a satisfactory agreement with the experimental measurements. Therefore, we focus now on the drag coefficient, using fixed values instead of Eq. (5). It is of prime importance to bear in mind that our aim is not to tune the prescribed value of C_d in order to obtain a good agreement with the experimental data. Our aim is to highlight the fact that there are

potentially strong inter-particle aerodynamic interactions causing a drag reduction that is not sufficiently well taken into account. Such interactions increase as droplets get close to each other. That is why we first discuss how dense the spray is, particularly close to the nozzle.

5.4.1 Calculation of the droplet volume fraction

As introduced in section 3.2, the drag reduction model in Eq. (8) is activated automatically when the local droplet volume fraction exceeds 10^{-5} by default in FDS. Fig. 10 (a) gives the time-averaged water mass per unit volume (MPUV) slice in the vertical mid-plane for the base case, with the range of $0 \sim 0.6\ \mathrm{kg}/m^3$, corresponding to the droplet volume fraction, α, of $0 \sim 6.0 \times 10^{-4}$. The contour line with the MPUV value of $10^{-2}\ \mathrm{kg}/m^3$, i.e., $\alpha = 10^{-5}$, is also shown for clarity by a black line. It is observed that the spray part with MPUV higher than $10^{-2}\ \mathrm{kg}/m^3$ is nearly identical to the spray shapes in Fig. 5 (a). This means that the drag reduction is considered within almost the entire spray in the FDS calculation. In Case 12, the drag reduction factor (DRF) is turned off during the calculation, and the spray width, d, presents a small increase of 0.04 m. The most important observation is that the automatic drag reduction function results in only a minor effect for the present spray.

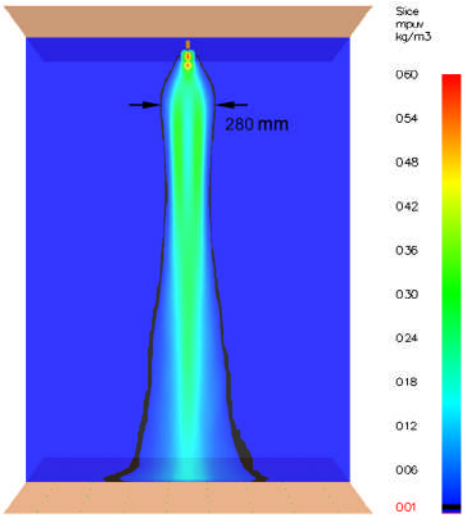

Fig. 10. Time-averaged water mass per unit volume (MPUV) slice in the vertical mid-plane for the base case. Black line: indication of the region within which the drag coefficient is automatically reduced.

In addition to the CFD simulation results discussed above, we also perform a simplified calculation here to support the hypothesis that the water spray at hand is

dense near the nozzle ($\alpha > 5.0 \times 10^{-4}$, see section 3.2). This method can also serve as a pre-calculation method to know, prior to advanced CFD calculations, if the spray is potentially dense and hence, if it requires “extra-care” with respect to drag force modelling (three-way coupling).

The basic idea consists of estimating the average water volume fraction near the nozzle:

$$\bar{\alpha} = \frac{V_{water\,(h)}}{V_{spray\ envelope\,(h)}} \qquad (12)$$

where $V_{water\,(h)}$ is the volume of water up to a distance h from the nozzle. Similarly, $\mathrm{V}_{\mathrm{spray\ enveloppe\ (h)}}$ is the volume of the spray envelope up to a distance h from the nozzle.

The volume of water up to a distance h from the nozzle can be expressed as:

$$V_{water\,(h)} = \dot{q} \cdot t_{(h)} \qquad (13)$$

where $\dot{q}$ is the water volume flow rate and $t_{(h)}$ is the time at which water droplets reach the distance h from the nozzle. Note that there is (almost) no evaporation for the case at hand.

At this stage, neither $t_{(h)}$ nor $\mathrm{V}_{\mathrm{spray\ enveloppe\ (h)}}$ are known a priori. They are calculated in the proposed method by solving Eq. (4) (in conjunction with Eq. (5) for the drag) for two droplets of 90 μm diameter each and with an initial velocity of 20 m/s. *Droplet 1* is given an angle of 42° in order to calculate the extent of the outer boundary of the spray. *Droplet 2* is given an angle of 0° in order to have an iso-contour of positions of droplets that were injected at the same time from the nozzle (as in Fig. 11).

Fig. 11 (a) shows that up to h= 0.15 m (corresponding to z = 2.05 m), the motion of *Droplet 1* is strongly influenced by its initial momentum and the drag force. Further downstream, gravity is dominant and all droplets in the spray fall vertically to the ground. The distance of h = 0.15 m is therefore taken as a reference distance for the calculation of the $\bar{\alpha}$. As shown in Fig. 11 (b), the half cone angle of the ball-cone is $42°$ and the radius, R, equals to $h \times \csc 42°$. Therefore, the corresponding spray envelope is $\mathrm{V}_{\mathrm{spray\ enveloppe\ (h)}} < V_{ball-cone} = 4.4 \times 10^{-3}\ m^3$ and $t_{(h)} = 0.114\ s$. Based on this information, $\bar{\alpha} > 4.3 \times 10^{-4}$ ($\approx 5 \times 10^{-4}$), which indicates that near the nozzle, the

spray could be regarded as a dense spray and the drag reduction effect between particles should be considered.

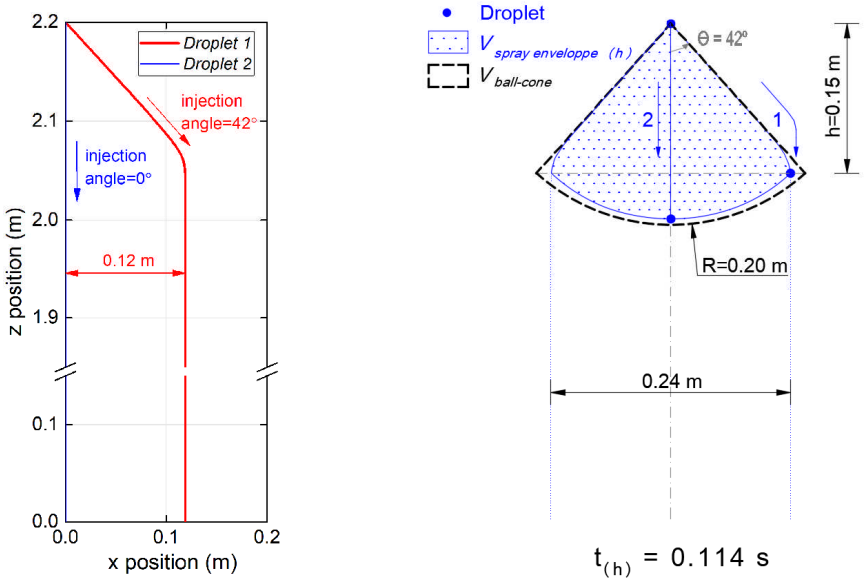

(a) The droplet trajectory (b) The schematic diagram of spray envelope ($t_{(h)} = 0.114\ s$)

Fig. 11. The droplet trajectory and the corresponding spray envelope using individual droplet (injected at z=2.2 m and landing at z=0 m).

5.4.2 Adjustments of the drag coefficient

Considering the significant under-prediction of the spray width in the simulations, compared to the experiments, it is interesting to investigate the impact of a reduction of the drag force on the water droplets. This is done in FDS by setting a constant drag value (instead of Eq.(5)) and performing a sensitivity analysis on the latter parameter. Based on Eqs. (5) and (5), the value of C_d increases from 0.94 to 18.11 during the droplet falling in Fig. 11 (a). Thus, to start, the C_d is assigned the minimum value of 0.94 in Case 13. Fig. 12 (a) illustrates that the spray in the far-field (away from the nozzle) is close to a cylinder with unchanged width, in contrast to the generally widening phenomenon in the base case (see Fig. 5 (a)) and Cases 1~12. This results in a slightly larger value for d (0.40 m) and a higher value for $\dot{q}''_{max}$ (5.93 $L/min/m^2$) on the ground, see Fig. 12 (b) and Table 2, when compared to the base case results. The reason for this is not clear yet, but more importantly, the substantial deviations from the experiments remain.

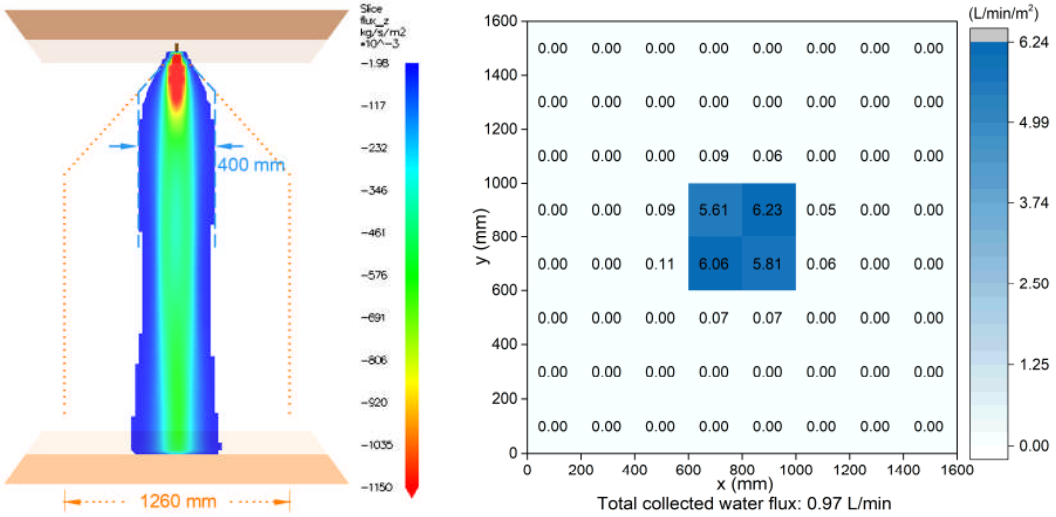

(a) Time-averaged water flux density slice (b) Flux density distribution on the ground

Fig. 12. The simulation results for Case 13 (fixed $C_d = 0.94$). The orange dashed lines denote the experimental results.

Next, Cases 14 to 25 were carried out to explore the effect of C_d in the simulation results, with the constant value decreasing from 3.0 to 0.1. As shown in Fig. 13 and Table 2, it is clear that the spray becomes wider with smaller C_d, with the deviation of d reducing from 90.5% to -27.0% continuously. In terms of the flux density distribution results, when C_d is set to values between 2.0 and 0.6 (Cases 15 to 20), the deviation of $\dot{q}''_{max}$ and $\dot{q}''$ remain nearly unchanged around -637.2% and 190.3%, respectively. As C_d continues to decrease below 0.6, the deviations of $\dot{q}''_{max}$ and $\dot{q}''$ both get smaller. As shown in Fig. 13, the deviations become 0 almost simultaneously around $C_d = 0.1 \sim 0.2$, to be considered as the optimum range for best agreement with the experimental results for the case at hand. Case 26 (with $C_d = 0.15$) has therefore been carried out. The same conclusion can be made from Fig. 14, showing the water flux density on the ground along the radial direction. The predicted spray shape in Fig. 15 (a) is very similar to the experimental one in Fig. 2 (b), although the spray width around 1.6 m is about 27% larger than the experimental result of 1.26 m. As mentioned in Fig. 2 (b), the spray width in the experiment was measured based on observation, which means the judgment of the spray boundary tends to be subjective. Therefore the 27% deviation could be accepted here. Fig. 15 (b) gives the flux density distribution result on the ground, with only around -54.0% and -24.3% deviation (see in Table 2) in $\dot{q}''_{max}$

and $\dot{q}''$, respectively, much smaller than the ones in the base case.

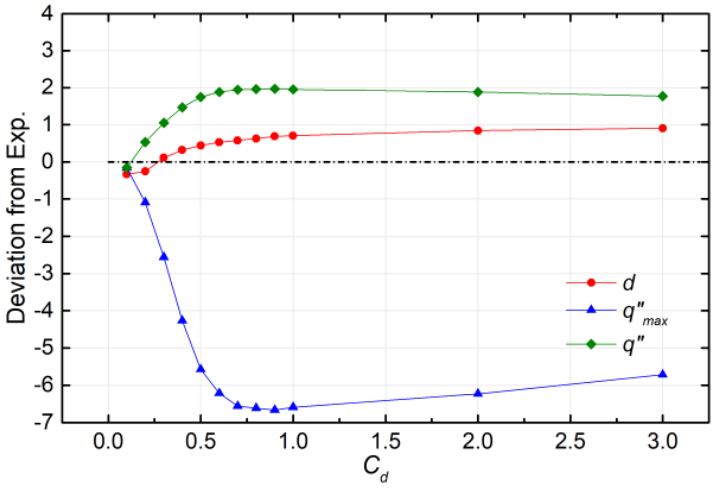

Fig. 13. Deviation of the simulation results from experimental results with different fixed values of C_d.

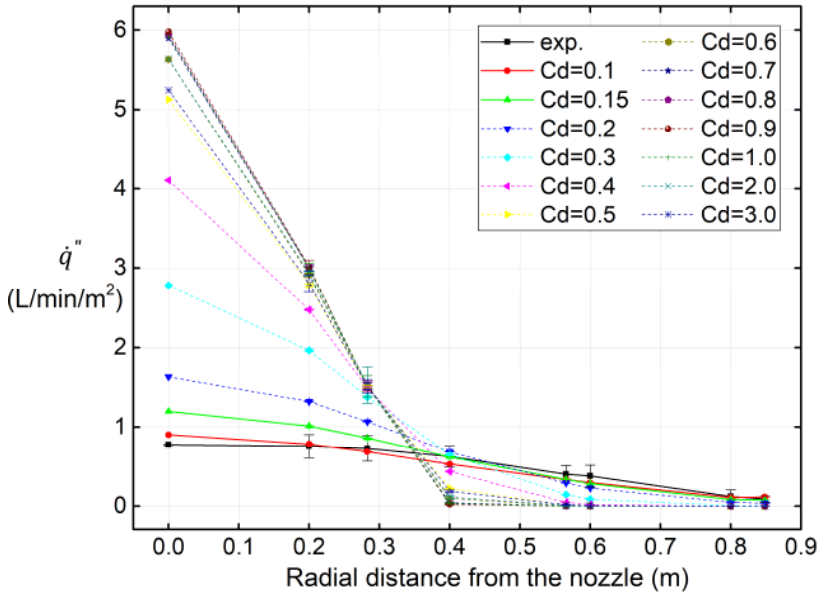

Fig. 14. Water flux density on the ground along the radial direction with different fixed values of C_d. *(The experimental data is also shown)*

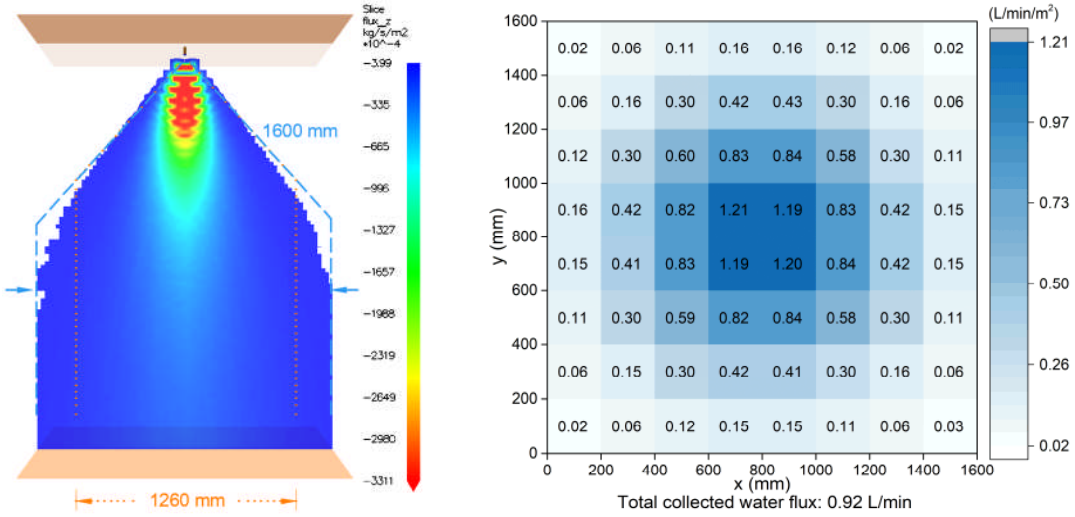

(a) Time-averaged water flux density slice (b) Flux density distribution on the ground

Fig. 15. The simulation results for Case 26 (fixed $C_d = 0.15$). The orange dashed lines denote the experimental results.

Therefore, the adjustment of the drag coefficient is shown to be key to obtain good agreement with the experimental data. Cases 27 and 28 have been carried out to explore the effect of the spray pattern shape and the turbulence model further, after the 'proper' adjustment of C_d. In terms of the spray pattern shape, Fig. 16 shows that a uniform angular distribution of water near the nozzle (i.e., uniform distribution) in combination with a constant Cd = 0.30 yields a water flux distribution on the ground that is similar to the combination Gaussian distribution and Cd = 0.15. Both numerical results are in good agreement with the experimental data. At this stage, it is difficult to be assertive regarding which of the two settings is the closest to reality. For that, more detailed measurements characterizing the spray near the nozzle are needed.

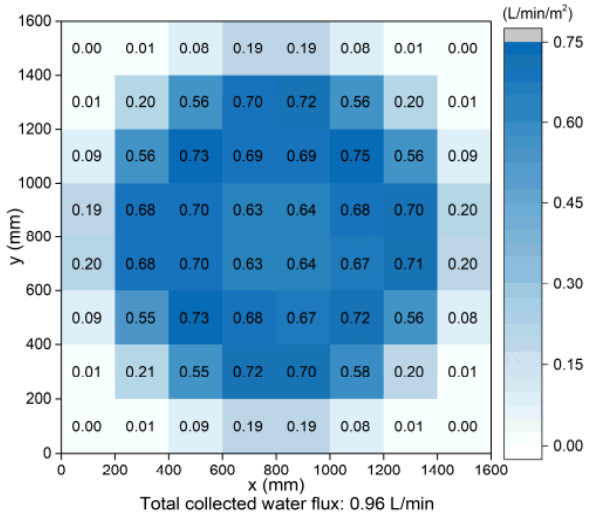

Fig. 16. The simulation result of the flux density distribution on the ground in Case 27 (a Uniform distribution, $C_d = 0.3$).

The simulation results with the dynamic Smagorinsky model (Case 28) are similar to the ones with the (default) modified Deardorff model (Case 26), comparing Fig. 17 and Fig. 15. The value of $C_d = 0.15$ is used in these two cases. This means the choice of the turbulence model has little effect on the simulation results for the present spray fixing the drag coefficient, and more importantly, that the choice in turbulence model is by far less influential than the drag force modelling.

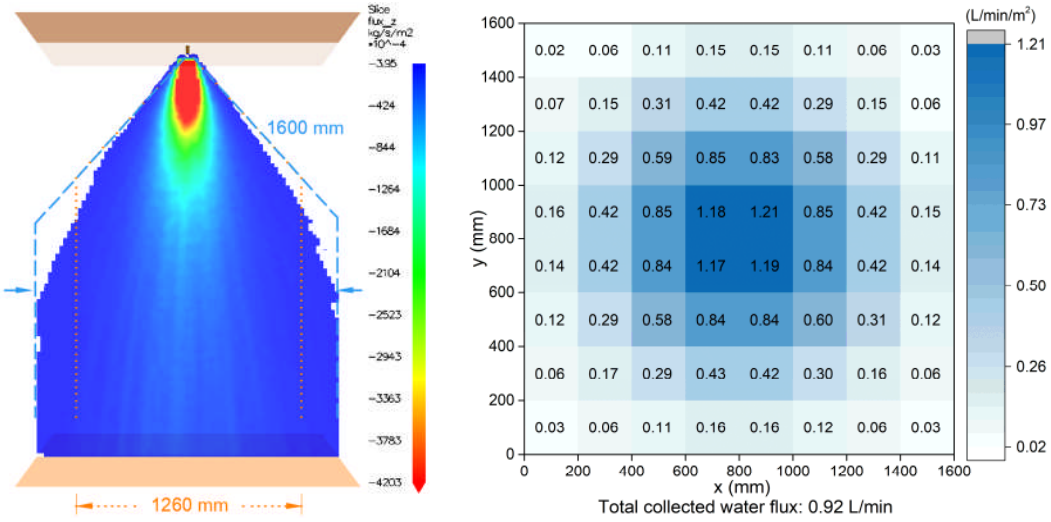

(a) Time-averaged water flux density slice (b) Flux density distribution on the ground

Fig. 17. The simulation results in Case 28 (the DS model, $C_d = 0.15$). The orange dashed lines denote the experimental results.

The modification of C_d as was done, knowing the outcome from the experiments, should not be solely viewed as a 'tuning exercise'. Obviously, the value of C_d = 0.15 should not be regarded as a 'universal constant' to be used for all sprays. Yet, the

563 results above emphasize the need for exploring new models to account for the drag
564 reduction effect in CFD calculations. Such models can be inspired by the results as
565 shown.

566 **6 Conclusion**

567 An extensive CFD simulation study has been performed on a water mist spray,
568 emerging from a nozzle positioned at 2.2 m above the ground, with a water flow rate
569 of 1.0 L/min under the pressure of 1.0 MPa. It is a solid cone spray, with spray half-
570 angle around $42°$ and droplet volume-median diameter about 90 μm.

571 A base case was set up to reproduce the experimental spray with the default
572 settings in the Fire Dynamics Simulator (FDS). However, substantial deviations to the
573 experiments appeared, in terms of the spray width near the nozzle, d, and the peak
574 water flux density on the ground, $\dot{q}''_{max}$, up to around 77.8% and -459.0%,
575 respectively. Therefore, a comprehensive set of numerical simulations have been
576 elaborated to investigate how to better reproduce the water mist spray at hand.

577 First, a detailed sensitivity analysis has been carried out on the numerical settings
578 (particle number injection rate and mesh cell size) and the injection settings (the initial
579 droplet velocity, the spray angle and the spray pattern shape). Substantial deviations
580 from the experimental results remained. While an impact was observed from the choice
581 of turbulence model, comparing results with dynamic Smagorinsky to results with the
582 default modified Deardorff model, also the turbulence model was illustrated not to be
583 the key to significantly improved agreement with the experimental data.

584 The main issue for the spray at hand is that it is a 'dense' spray (near the nozzle).
585 This was argued on the basis of the droplet volume fraction from the CFD results, but
586 also through a simplified calculation method, which can in general be done prior to the
587 start of the CFD simulations, based on 2 individual droplets. This indicated that the
588 drag reduction effect between droplets should be considered in the spray. The built-in
589 calculation for the drag reduction effect by default in FDS does not lead to satisfactory
590 results for the case at hand. Hence, C_d has been fixed, to a range of values between

3.0 and 0.1. The results show that an accurate numerical representation of the spray at hand can be achieved when $C_d = 0.1 \sim 0.2$ for the case at hand. The modification of C_d as was done, knowing the outcome from the experiments, should not be solely viewed as a 'tuning exercise'. Obviously, the value of C_d = 0.15 should not be regarded as a 'universal constant' to be used for all sprays. This study emphasizes the need for exploring new models for the drag reduction effect in CFD calculations of dense sprays. Ideally, the development of such models would be supported by experimental measurements of C_d in simplified 'canonical' configurations by tracking a limited number of droplets.

The work also lays the groundwork for further simulations on the interaction between multiple sprays, as is the case for the water mist system with more than one nozzle. These aspects will be explored in follow-up studies.

Acknowledgements

This research was funded by National Natural Science Foundation of China (NSFC) under Grant No. 51508426 and Grant No. 51576144, and China Scholarship Council [grant No. 201606270109]. Martin Thielens is a PhD student who holds a grant for fundamental research from the Fund of Scientific Research – Flanders (FWO – Vlaanderen). The FWO file number of his mandate is 1182919N.

References

[1] Hurley MJ, SFPE Handbook of Fire Protection Engineering, 2016.

[2] G. Grant JB, D. Drysdale, Fire suppression by water sprays, 2000.

[3] Jenft A, Collin A, Boulet P, Pianet G, Breton A, Muller A, Experimental and numerical study of pool fire suppression using water mist, Fire Safety Journal, 2014;67: 1-12.

[4] Kim SC, Ryou HS, An experimental and numerical study on fire suppression using a water mist in an enclosure, Building and Environment, 2003;38: 1309-16.

[5] Ferng Y-M, Liu C-H, Numerically investigating fire suppression mechanisms for the water mist with various droplet sizes through FDS code, Nuclear Engineering and Design, 2011;241: 3142-48.

[6] Prasad K, Li C, Kailasanath K, Simulation of water mist suppression of small scale methanol liquid pool fires, Fire Safety Journal, 1999;33: 185-212.

[7] Prasad K, Patnaik G, Kailasanath K, A numerical study of water-mist suppression of large scale compartment fires, Fire Safety Journal, 2002;37: 569-89.

[8] Husted BP. Experimental measurements of water mist systems and implications for modelling in

CFD. Lund University, Sweden, 2007.

[9] Beji T, Zadeh SE, Maragkos G, Merci B, Influence of the particle injection rate, droplet size distribution and volume flux angular distribution on the results and computational time of water spray CFD simulations, Fire Safety Journal, 2017;91: 586-95.

[10] Sikanen T, Vaari J, Hostikka S, Paajanen A, Modeling and Simulation of High Pressure Water Mist Systems, Fire Technology, 2014;50: 483-504.

[11] Mahmud HMI, Moinuddin KAM, Thorpe GR, Experimental and numerical study of high-pressure water-mist nozzle sprays, Fire Safety Journal, 2016;81: 109-17.

[12] Sikanen T. Simulation of transport, evaporation, and combustion of liquids in large-scale fire incidents. Department of Civil Engineering, Aalto University, 2017.

[13] Zapryagaev VI, Kudryavtsev AN, Lokotko AV, Solotchin AV, Hadjadj A. An experimental and numerical study of a supersonic-jet shock-wave structure. In. An experimental and numerical study of a supersonic-jet shock-wave structure. RUSSIAN ACADEMY OF SCIENCES NOVOSIBIRSK INST OF THEORETICAL AND APPLIED …, 2002.

[14] Bray M, Cockburn A, O'Neill W, The Laser-assisted Cold Spray process and deposit characterisation, Surface and Coatings Technology, 2009;203: 2851-57.

[15] Yin S, Meyer M, Li W, Liao H, Lupoi R, Gas Flow, Particle Acceleration, and Heat Transfer in Cold Spray: A review, Journal of Thermal Spray Technology, 2016;25: 874-96.

[16] Samareh B, Stier O, Lüthen V, Dolatabadi A, Assessment of CFD modeling via flow visualization in cold spray process, Journal of Thermal Spray Technology, 2009;18: 934.

[17] Ko YJ. A Study of the Heat Release Rate of Tunnel Fires and the Interaction between Suppression and Longitudinal Air Flows in Tunnels. 2011.

[18] NFPA. NFPA 750, Standard on Water Mist Fire Suppression Systems. In. NFPA 750, Standard on Water Mist Fire Suppression Systems. Quincy, MA, National Fire Protection Association, 1996.

[19] In. https://github.com/firemodels/fds/releases/tag/FDS6.6.0.

[20] McGrattan; K, Hostikka; S, McDermott; R, Floyd; J, Weinschenk; C, Overholt; K. Fire Dynamics Simulator Technical Reference Guide Volume 1: Mathematical Model. In. Fire Dynamics Simulator Technical Reference Guide Volume 1: Mathematical Model. 2013.

[21] McGrattan; K, Hostikka; S, McDermott; R, Floyd; J, Vanella; M, Weinschenk; C, Overholt; K. Fire Dynamics Simulator, User Guide, National Institute of Standards and Technology, NIST Special Publication 1019 6th Edition. In. Fire Dynamics Simulator, User Guide, National Institute of Standards and Technology, NIST Special Publication 1019 6th Edition. Gaithersburg, MD, 2013.

[22] Salewski M, Fuchs L, Effects of aerodynamic particle interaction in turbulent non-dilute particle-laden flow, Journal of Turbulence, 2008;9: N46.

[23] Elghobashi S, On predicting particle-laden turbulent flows, Applied Scientific Research, 1994;52: 309-29.

[24] Sommerfeld; M, Wachem; Bv, Oliemans; R, Best particle guidelines for Computational Fluid Dynamics of dispersed multiphase flows, 2008.